Proceedings of ASME Turbo Expo 2019
Turbomachinery Technical Conference and Exposition
GT2019
June 17-21, 2019, Phoenix, Arizona, USA

GT2019-90977

INVESTIGATION OF MIXED MICRO-COMPRESSOR CASING TREATMENT USING NON-MATCHING MESH INTERFACE

Purvic Patel*
Gecheng Zha†
Department of Mechanical and Aerospace Engineering
University of Miami
Coral Gables, Florida 33124
Email: gzha@miami.edu

ABSTRACT

In this paper, a non conservative interpolation boundary condition, for the non-matching mesh blocks, was developed and validated for the micro compressor casing treatment. The conservative variables were interpolated in the halo layers of non-matching mesh interface using Finite Element Method (FEM) type linear interpolation shape functions, instead of using over-set grids. Using this new boundary condition, the effect of casing treatment on stall margin and compressor performance is investigated for a mixed flow type micro-compressor. The computed compressor performance map for the casing treatment case is compared with the experimental results and shows good agreement except in the region close to stall. With the application of the casing treatment, improvement in the stall margin is observed without the loss of efficiency over the operating range.

NOMENCLATURE

L_{ref}	Reference length
d_w	Wall normal distance
ρ_∞	Freestream density
U_∞	Freestream velocity
μ_∞	Freestream dynamics viscosity
Ω	Vorticity
W_t	Tangential velocity in relative frame
V_t	Tangential velocity in absolute frame
V_m	Meridional velocity
β	Relative flow angle$= \tan^{-1}(-W_t/V_m)$
α	Absolute flow angle$= \tan^{-1}(V_t/V_m)$
Re	Reynolds number
SS	Suction Surface
PS	Pressure Surface
SA	Spalart-Allmaras
B.C.	Boundary Condition
CT	Casing Treatment
MUSCL	Monotonic Upwind Scheme for Conservation Laws
CFD	Computational Fluid Dynamics
FEM	Finite Element Method

INTRODUCTION

Aviation industry is constantly striving to increase the aerodynamic efficiency of aircraft and thereby reducing the fuel consumption and its emission pollution. High lift and low drag wing design is one of the crucial requirements of aircraft design. Active flow control is considered as a promising direction to improve the airfoil performance. Zha et al. [1–4] have developed Co-Flow Jet active flow control airfoil, which is demonstrated to achieve very high lift coefficient, reduce drag, and also improve the cruise efficiency. One of the vital component of Co-Flow Jet technology is the micro-compressor actuator to draw a mass flow near the trailing edge, pressurize it and eject the flow near

*Ph.D. Student
†Professor, ASME Fellow

the leading edge. As this compressor needs to work under various operating conditions during take-off, cruise and landing, its design needs to encompass wide operating range with high efficiency.

Over the last two decades, aircraft engine compressors and fans are designed with increased loading to reduce the size and weight. This brings more attention to the study of effects of increased blade tip loading. Blade tip loading plays an important role to the tip vortex, which is one of the primary source of stall inception. The tip vortex trajectory normal to the main flow is considered as near stall operating point. Low-momentum tip vortex near the rotor tip leading edge causes flow spillage and leads to stall inception [5]. It is observed that the extraction of this low axial momentum flow and reinjection of the same in the main flow with Casing Treatment (CT) helps to improve the stall margin of compressors [6, 7].

Various designs of Casing Treatment (CT) are devised, including circumferential grooves CT [8], non-axisymmetric slot-type CT [9], honeycomb CT [10], self-recirculating flow channels [6, 11], ported shroud casing treatment [7] and multiple cylindrical hole casing treatment (MHCT) [12]. In the early development, researchers found that apart from enhancing operating range, they brought penalty mostly in the form of efficiency. In order to mitigate the efficiency penalty, over the time various CT designs have been proposed and investigated to understand their effect on the tip leakage flow and thereby its influence on the main passage flow.

Based on Khalid [10], the use of flow aligned honeycomb casing treatment gives higher stall margin than the circumferential grooves as it helps to absorb tangential energy in the flow and enhances streamwise flow momentum by aligning flow more axially. Hathaway [6] showed the concept of the self-recirculating casing treatment to increase the stall margin with minimal or no decrement to efficiency, where pressure difference across the CT acts as a driving force for fluid movement and the direction of flow in CT is determined by high pressure side of CT. Chen et al. [7] demonstrated that the use of ported CT design for centrifugal compressor can enhance stall margin by reducing the strength of shock on the blade suction surface and removal of low momentum flow due to recycling it by port CT. Yang et al. [12] investigated the effect of extraction hole area and its location on transonic axial compressor stability margin. Based on their findings, penalty on the compressor pressure ratio and efficiency is influenced by the amount of recirculation flow governed by the size of extraction hole and its location. In general, CT design needs to reduce accumulation of low momentum area and move the trajectory of tip vortex from circumferential to axial in order to delay stall inception. Most of the previous CT studies are focused on aircraft engine compressors with high Reynolds number.

Recently, with the growing importance of active flow control for aircraft performance, micro-compressors used as actuators for active flow control open a new area of research and applications [13]. The micro-compressors usually have the diameters in the order of less than 8 cm, which brings the Reynolds number in the order of 50,000 or less. The small Reynolds number make the flow prone to separation and make the compressor prone to stall. Casing treatment to extend the operating range of micro-compressors are hence very important. The other feature of micro-compressors is that they are often designed as mixed type to take the advantage of the compactness of centrifugal compressors and high mass flow rate of axial compressors. Few casing treatment studies for mixed micro-compressors are seen in literatures.

In the present research, the casing treatment of a mixed micro-compressor is simulated and investigated. The casing treatment comprises of multiple cylindrical channels to extract flow from casing and collection chamber. Numerical investigation of such CT design requires generation of high quality grid. Grid clustering and proper smoothness have remained nettlesome task for the solution of 3D Navier-Stokes equations.

With the increasing geometric complexity, creating structured conformal mesh is becoming increasingly difficult and sometimes prohibitive. This leads to the development of grid-embedding or overset grid technique. Benek et al. [14] developed chimera grid-embedding method allowing more flexibility to generate boundary-conforming grids on components part of geometry, refining mesh in the region of interest, and allowing different flow model solution on different grid. This method in the original form uses non-conservative trilinear interpolation scheme. Kao et al. [15] developed Dragon grid, which is a hybrid grid scheme preserving the strength of Chimera grid, and at the same time preserving conservation of conservative properties by embedding unstructured grid in the hole region of Chimera grid. Fenwick et al. [16] implemented FEM like halo layer interpolation. This paper is intended to develop a general numerical strategy to simulate any type of compressors casing treatments. A mixed micro-compressor casing treatment is investigated due to the scarcity of the research in this area and its extremely high importance for active flow control.

The objective of this paper is to introduce a new FEM type interpolation boundary condition across the interface between the CT channel and compressor flow path with non-matching mesh, which is non-conservative. The advantage of this method is its convenience to treat casing treatment without matching mesh across interface for flux conservation, but it still achieves a fairly good accuracy as to be demonstrated. The major difference between Fenwick's implementation and the present one lies in the way of searching halo cells position and determining their associated weights, which are mentioned later on. The present implementation is validated with the experimental results of a mixed micro-compressor with self recirculating casing treatment. Using this non-matching mesh interface treatment, the effect of the self-recirculating casing treatment on the mixed

micro-compressor stability and its performance is studied.

GOVERNING EQUATIONS IN GENERALIZED COORDINATES

The in-house CFD solver, originally developed by the CFD and Aerodynamics lab at the University of Miami, is used in the present research. The Favre-averaged RANS equation along with one equation Spalart-Allmaras (SA) turbulence model are solved in fully coupled manner using an implicit unfactored Gauss-Seidel line iteration to achieve high convergence rate. The Favre-averaged RANS equations are nondimensionalized using L_{ref}, ρ_∞, U_∞ and μ_∞ and their differential form in generalized coordinates are given by:

$$\frac{\partial Q}{\partial t}+\frac{\partial E}{\partial \xi}+\frac{\partial F}{\partial \eta}+\frac{\partial G}{\partial \zeta}=\frac{1}{Re}\left[\frac{\partial R}{\partial \xi}+\frac{\partial S}{\partial \eta}+\frac{\partial T}{\partial \zeta}\right]+S_v \qquad (1)$$

where,

$$Q=\frac{1}{J}\begin{bmatrix}\rho\\ \rho u\\ \rho v\\ \rho w\\ \rho e\\ \rho\hat{\nu}\end{bmatrix}, E=\frac{1}{J}\begin{bmatrix}\rho U\\ \rho uU+p\xi_x\\ \rho vU+p\xi_y\\ \rho wU+p\xi_z\\ (\rho e+p)U\\ \rho\hat{\nu}U\end{bmatrix}, F=\frac{1}{J}\begin{bmatrix}\rho V\\ \rho uV+p\eta_x\\ \rho vV+p\eta_y\\ \rho wV+p\eta_z\\ (\rho e+p)V\\ \rho\hat{\nu}V\end{bmatrix}$$

$$G=\frac{1}{J}\begin{bmatrix}\rho W\\ \rho uW+p\eta_x\\ \rho vW+p\eta_y\\ \rho wW+p\eta_z\\ (\rho e+p)W\\ \rho\hat{\nu}W\end{bmatrix}, R=\frac{1}{J}\begin{bmatrix}0\\ \tau_{xi}\xi_i\\ \tau_{yi}\xi_i\\ \tau_{zi}\xi_i\\ (u_j\tau_{ij}-q_i)\xi_i\\ \frac{\rho}{\sigma}(\nu+\hat{\nu})\frac{\partial\hat{\nu}}{\partial x_i}\xi_i\end{bmatrix}$$

$$S=\frac{1}{J}\begin{bmatrix}0\\ \tau_{xi}\eta_i\\ \tau_{yi}\eta_i\\ \tau_{zi}\eta_i\\ (u_j\tau_{ij}-q_i)\eta_i\\ \frac{\rho}{\sigma}(\nu+\hat{\nu})\frac{\partial\hat{\nu}}{\partial x_i}\eta_i\end{bmatrix}, T=\frac{1}{J}\begin{bmatrix}0\\ \tau_{xi}\zeta_i\\ \tau_{yi}\zeta_i\\ \tau_{zi}\zeta_i\\ (u_j\tau_{ij}-q_i)\zeta_i\\ \frac{\rho}{\sigma}(\nu+\hat{\nu})\frac{\partial\hat{\nu}}{\partial x_i}\zeta_i\end{bmatrix} \qquad (2)$$

The viscous term vectors R, S, and T are represented in indicial notations, using dummy indices i and j, in Equation (2). In Equation (1) S_v represents the SA turbulence model source term vector. Apart from using SA-noft2 [17] turbulence model, modifications [17, 18] for SA turbulence model production term are used to avoid numerical difficulties arising from $\hat{S}$ reaching to zero or becoming negative. Production term modifications for SA turbulence model are given by:

$$\overline{S}=\frac{1}{Re}\frac{\hat{\nu}}{\kappa^2 d_w^2}f_{v2} \qquad (3)$$

$$\hat{S}=\begin{cases}\Omega+\overline{S} & :\overline{S}\geq -c_2\Omega\\ \Omega+\frac{\Omega(c_2^2\Omega+c_3\overline{S})}{(c_3-2c_2)\Omega-\overline{S}} & :\overline{S}<-c_2\Omega\end{cases} \qquad (4)$$

where, $c_2=0.7$, $c_3=0.9$ and set $r=10$ if $\hat{S}=0$.

Details of the standard SA turbulence model implementation can be found in reference [19].

NON-MATCHING MESH INTERFACE INTERPOLATION

A schematic two dimensional non-matching mesh interface is shown in Figure 1. Two halo layers are generated across the interface which can allow the use of higher order schemes requiring upto five point stencil. In the case of matching interface at internal block boundary, halo layers can assume the position easily as opposed to the situation here. In the present method, the halo layers for block A are generated by marching in the direction (i.e. ξ ,η or ζ) into block B with a distance determined by the first layer of block B's mesh at the interface, vice versa.

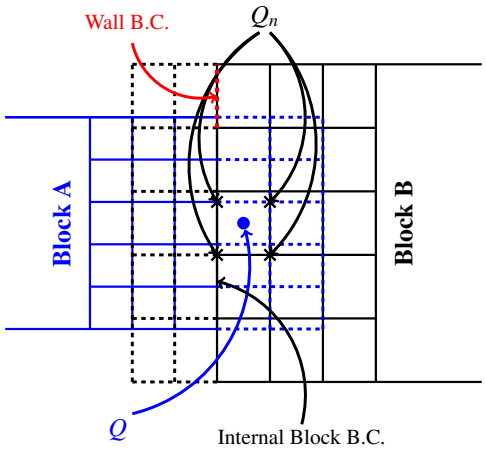

FIGURE 1: Non-matching mesh

(- - - - Mesh A halo layer, and - - - - Mesh B halo layer)

The algorithm for assuming conservative variables at the cell center of halo layers is as below:

1 Block A halo layer control volume center position coordinates are represented in terms of the nearest eight vertex of

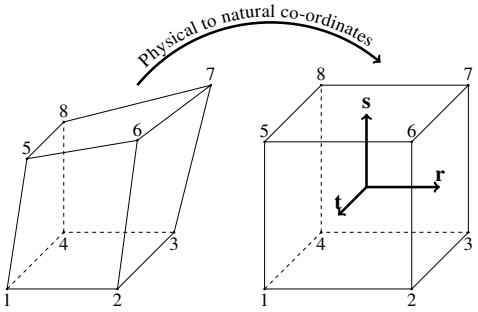

FIGURE 2: Physical to Natural co-ordinates conversion

block B by

$$\begin{bmatrix} x \\ y \\ z \end{bmatrix}_{halo}^{A} = \sum_{i=1}^{8} N_i \begin{bmatrix} x \\ y \\ z \end{bmatrix}_{i}^{B} \tag{5}$$

where N_i are the eight-node brick element FEM shape functions (Equation (6)) [20]. Equation (5) represents non-linear equations in terms of r, s and t, which are solved by Newton-Raphson method for simultaneous non-linear equations. Values of natural coordinates range between -1 to 1. Their values help to create connectivity matrix. This matrix contains the information of halo layer mesh element connection to physical mesh element of another block, and value of shape functions. Similar procedure is carried out for Block B halo layer control volume center position coordinates.

$$\begin{aligned}
N_1 &= \frac{1}{8}(1-r)(1-s)(1+t) \\
N_2 &= \frac{1}{8}(1+r)(1-s)(1+t) \\
N_3 &= \frac{1}{8}(1+r)(1-s)(1-t) \\
N_4 &= \frac{1}{8}(1-r)(1-s)(1-t) \\
N_5 &= \frac{1}{8}(1-r)(1+s)(1+t) \\
N_6 &= \frac{1}{8}(1+r)(1+s)(1+t) \\
N_7 &= \frac{1}{8}(1+r)(1+s)(1-t) \\
N_8 &= \frac{1}{8}(1-r)(1+s)(1-t)
\end{aligned} \tag{6}$$

2 The shape function (N_i) is evaluated using the calculated natural coordinates and this serves as weight function for the conservative variable interpolation.

3 Values of conservative variables are extrapolated to cell vertex for the first two layers of physical mesh near the interface for both blocks. In the case of reference frame change, this extrapolated values are calculated in the stationary frame.

3 Once the N_is are known, conservative variables at control volume center of Block A halo mesh are interpolated using nearest eight vertex conservative variable values of block B physical mesh using

$$\left[Q\right]_{halo}^{A} = \sum_{i=1}^{8} N_i \left[Q_n\right]_{i}^{B} \tag{7}$$

Conservative variables in Block B halo layers are searched following similar procedure. Once the value of both block halo layers are found with interpolation, they are recalculated to take into account their original frame of reference, in case of reference frame change.

The wall boundary condition is placed for the halo layer cell center which are not within any cell in the other block (Figure 1). At the time of finding the connectivity matrix, if the wall BC is placed for any cell, nearest wall distance values need to be recalibrated to account for the proper destruction and production terms in SA turbulence model.

In the case of Fenwick's implementation, halo layer control volume center position is determined by nearest eight cell center position as compared to the present one. So in his implementation weights are calculated at nearest eight cell center whereas here weights are calculated at grid points. As the value of the conservative variables in the halo cells are assumed based on its cell center position in other block, the flux at the non-matching mesh interface is not conserved. This method is relatively simple to implement and requires less computational efforts, as it does not require to find overlapping areas between cells at an interface like in a conservative interpolation.

COMPUTATIONAL SETUP

Computational Grid

In the present study only structured mesh is used. Single blade passage used for the numerical simulation is highlighted in the full annulus mesh overview (Figure 3(a)).

O-mesh topology is used around all the blades (Figures 3(b) to 3(d)) as it ensures highly orthogonal grid near the wall and thereby reducing grid skewness. Rotor tip clearance is fully gridded with O-mesh topology and 11 grid points in radial direction. In the CT circular channel, the butterfly topology is used as shown in Figure 3(b). Inlet, outlet and collection chamber of CT are modeled using H-mesh topology. The region between diffuser and OGV domain is gridded with the H-grid topology.

Table 1 provides the overview of number of grid points in the direction around blade (i), blade to blade (j), and spanwise

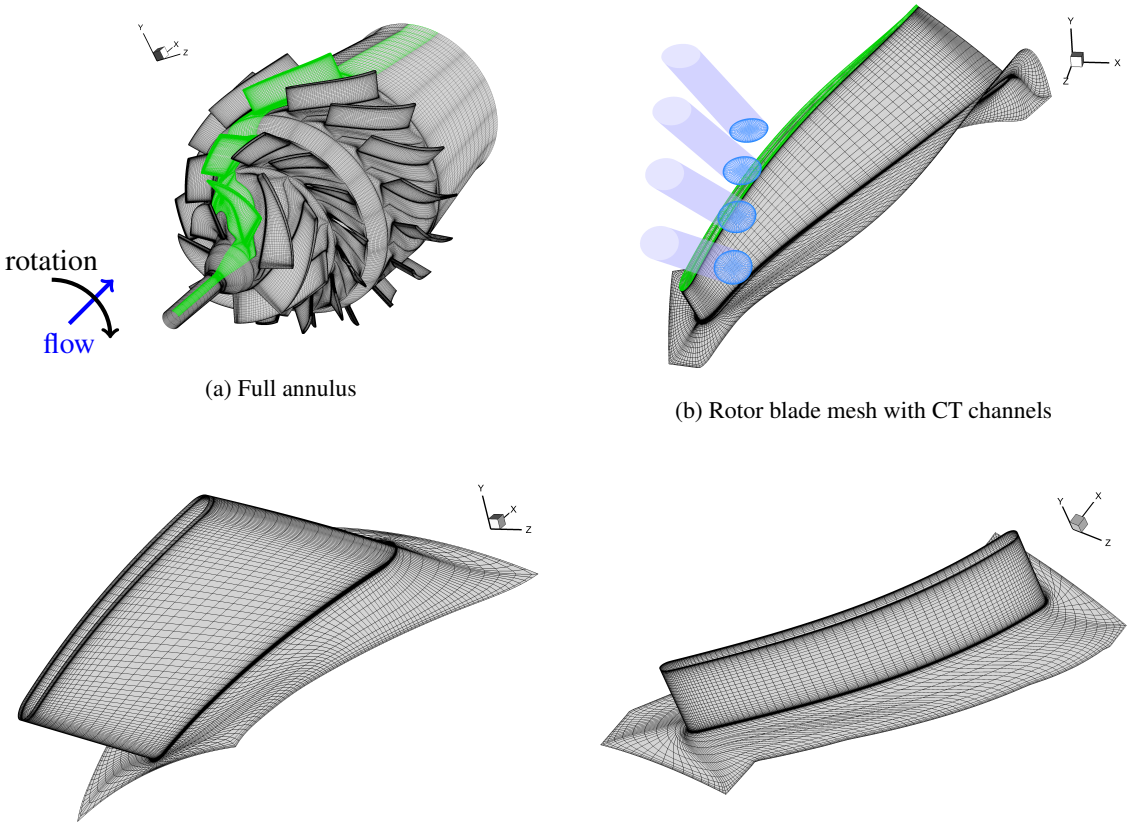

(a) Full annulus

(b) Rotor blade mesh with CT channels

(c) Diffuser blade mesh

(d) OGV mesh

FIGURE 3: Mesh overview

Domain	$i \times j \times k$
Rotor	$229 \times 51 \times 51$
Diffuser vane	$189 \times 42 \times 51$
OGV	$181 \times 42 \times 51$
Rotor tip block	$229 \times 13 \times 11$

TABLE 1: Grid points around blade

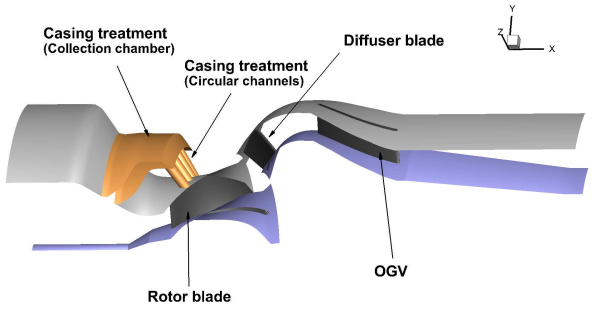

FIGURE 4: Single blade passage geometry

(k), respectively for the all the blades. The total number of cells is 1,753,760.

Boundary conditions (BCs)

Figure 4 shows micro-compressor simulated in the present study, which consists of inlet duct with a rotor, followed by diffuser and outlet guide vanes (OGV) with an outlet duct. For the numerical simulation purpose of the compressor with CT, additional domain of 1.5 times the rotor hub chord length is added at the upstream of inlet duct. However, all the measurements in the numerical simulation are carried out without the additional domain so that the results are more comparable with the experi-

mental results. As shown in Figure 4, the casing treatment of this compressor is implemented by four circular channels located at about 14% tip chord from the tip blade leading edge. The four channels are extended radially and are connected to a chamber, which reaches the wall of the compressor inlet. Such a configuration allows the flow at the rotor casing to travel to the inlet to extend the stall margin.

Stagnation quantities (i.e. total pressure and total temperature) and flow angles are specified at the inlet. A velocity component is extrapolated from the inner domain to determine the remaining flow variables at the inlet boundary. At the outlet, static pressure is specified with radial equilibrium BC. Since the flow is subsonic, remaining flow variables are extrapolated from the inner domain at outlet boundary condition. On the blade surface and CT cylindrical channel wall no-slip wall boundary condition is used, whereas the remaining walls are modeled with an efficient wall BC [21], which switches from no-slip wall BC to wall function BC if y^+ is between 11 to 300. Zero heat flux through the wall is imposed by an adiabatic equation. The non-matching mesh interface BC, described earlier, is applied on the interface between rotor casing and CT cylindrical channel, and between the CT cylindrical channel and CT collection chamber. Periodic boundary conditions are applied on the sides of single blade passage domain. Mixing plane boundary is used between two blade rows.

Numerical Methods

The steady state Favre-averaged RANS equations described by Equation (1) are solved using finite control volume method. The Roe flux difference scheme [22, 23] is used to evaluate the inviscid flux, where left and right hand side conservative variables required at the control volume interface are reconstructed using the 3^{rd} order *MUSCL* scheme [24], and the 2^{nd} order central differencing scheme is used for the viscous flux in the present study. In order to save wall clock time, high-scalability parallel computing is used [25].

RESULTS ANS DISCUSSION

Compressor characteristics

Figure 5 shows the computed compressor characteristics compared with the measurement data [26, 27] at design speed for both with and without CT for the same micro-compressor. At the design speed, the compressor is rotating at 115,000 rpm with the tip diameter of 39.76 mm. It should be noted that the measurement data is only available for the compressor with CT. In the experiment, gate valve is used at the outlet to obtain the different operating points along the speedline.

In Figure 5(a), the abscissa represents the non dimensional mass flow rate and the ordinate represents the total-to-static pressure ratio. This total-to-static pressure ratio is obtained from the

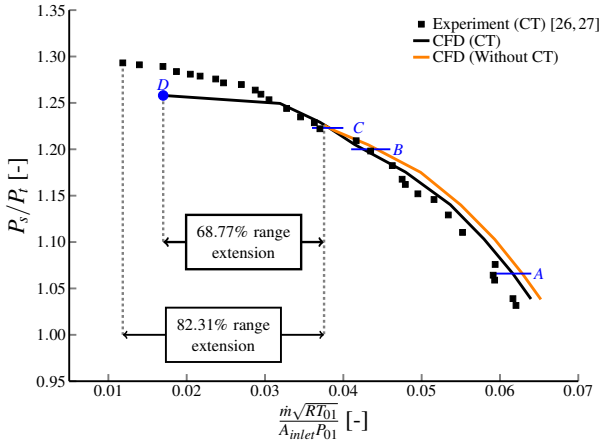

(a) Speed line - Pressure ratio

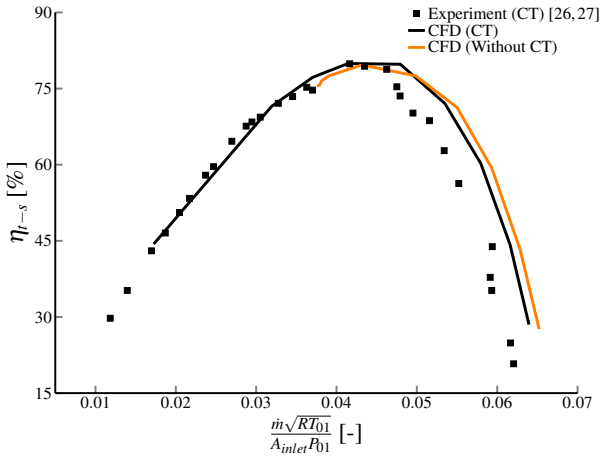

(b) Speed line - Isentropic efficiency

FIGURE 5: Micro compressor characteristics at design speed

mass flow averaged static pressure (P_s) at the outlet and the total pressure (P_t) at the inlet. In Figure 5(b), the ordinate represents the total-to-static isentropic efficiency obtained from the mass flow averaged total and static quantities at the inlet and outlet section. It is observed that near the choke point, the CT leads to a small reduction in mass flow rate. As the back pressure is increased towards the design point, the discrepancy in the mass flow rate between both the cases is reduced. Excellent agreement is found for total-to-static pressure ratio whereas the total-to-static isentropic efficiency is over predicted by the numerical simulation near the choke side as compared to the experimental results. This over prediction of the isentropic efficiency is attributed to the prediction of the extent of separation in blade rows at off-design points. As experimental results are only available across the compressor stage, it is difficult to say which blade row is under-predicting the flow separation. The predicted peak

efficiency for both the numerical simulation cases are close to the one measured in experiment. As shown in Figure 5, the CT is found to allow significant increase in the operating range of compressor as compared to the one without CT. For the CT compressor, the numerical simulation fails to predict a lower operating range as measured and also under-predicts the pressure ratio at the low mass flow near stall range. The reason for the difference between CFD and experimental stall mass flow rate can be attributed to the unsteady flow generated by CT which needs to be further investigated with the unsteady simulation.

Figure 5(a) indicates a significant increase in mass flow range by the CT relative to the smooth wall mass flow range, similar to the observation for self-recirculation CT by Hathaway [6]. The numerical simulation predicts a mass flow range extension of 68.77%, which is underpredicted by about 13%. Overall, a significant range extension is gained with casing treatment over the case without casing treatment. Four Points A, B, C and D marked in pressure ratio characteristic speed line are the near choke point ($Ps/Pt = 1.066$), the near design point ($Ps/Pt = 1.205$), the near stall point for the compressor without CT ($Ps/Pt = 1.22$) and the near stall point for the compressor with CT ($Ps/Pt = 1.26$), respectively. At points A, B and C, radial profiles and blade tip loading will be compared subsequently.

Effect of non-conservative interpolation

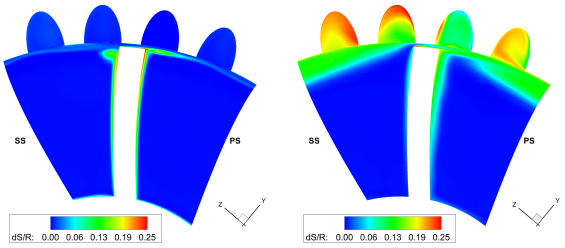

(a) $Ps/Pt = 1.066$ (b) $Ps/Pt = 1.22$

FIGURE 6: Discontinuity in entropy

Non-conservative interpolation is comparatively easier to implement than the conservative interpolation. As the fluxes are not conserved across the interface, it generates non-smooth entropy creation as shown in Figure 6, which is the entropy contours showing the variation in the CT channels and rotor. However, no significant effect on the overall compressor performance is observed.

Casing treatment flow

Figures 7 to 10 illustrate the static pressure contour for the inlet duct, rotor, CT channels and chamber with the increase in

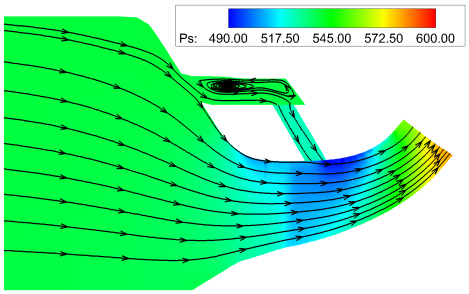

FIGURE 7: Meridional view at $Ps/Pt = 1.066$, Point A

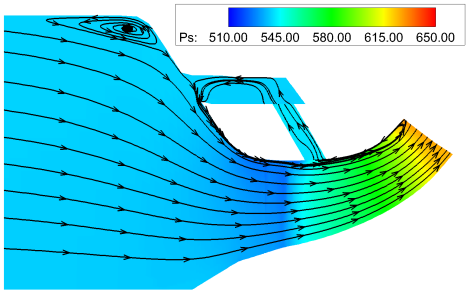

FIGURE 8: Meridional view at $Ps/Pt = 1.205$, Point B

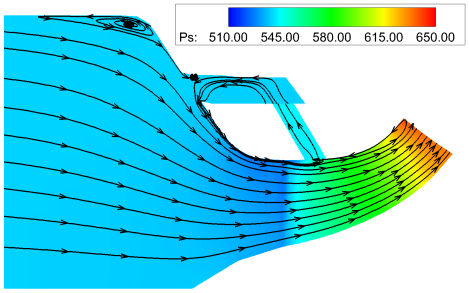

FIGURE 9: Meridional view at $Ps/Pt = 1.22$, Point C

pressure ratio from the near choked to the near stall point as marked by A, B, C and D in Figure 5(a). This meridional plane contour is obtained by the pitch-wise averaging. The discontinuity at the non-conservative interface in the meridional view is due to the circumferential averaging over the wall and internal boundary region for the rotor casing and CT chamber. In the self-recirculating CT, pressure gradient across the inlet and outlet of

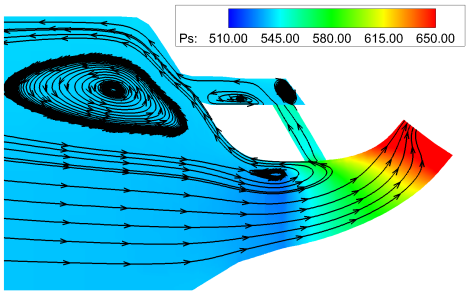

FIGURE 10: Meridional view at $Ps/Pt = 1.26$, Point D

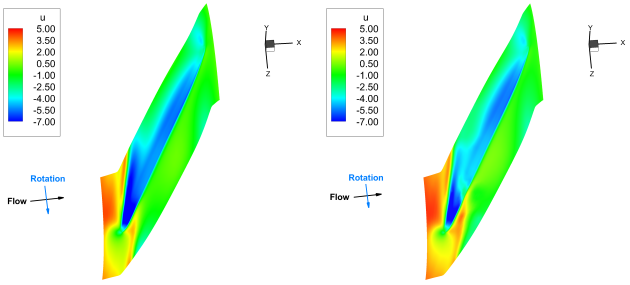

(a) Without CT (b) With CT

FIGURE 11: Axial velocity at 98.5% span for $Ps/Pt = 1.22$

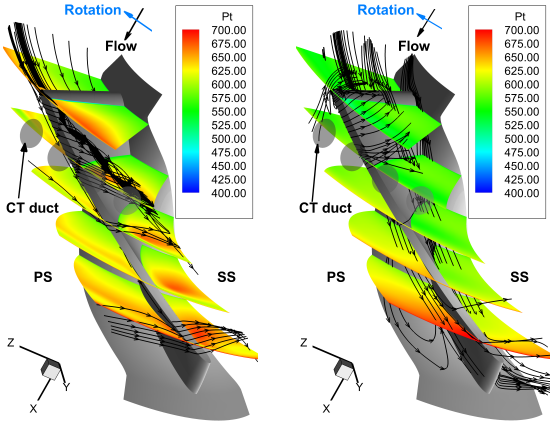

(a) At $Ps/Pt = 1.22$ (b) At $Ps/Pt = 1.26$

FIGURE 12: Tip leakage trajectory for Compressor with CT

CT is the driving force for the recirculating flow. Near the choke (point A in Figure 5(a)) due to the low tip pressure, the flow is driven from the compressor inlet to the rotor tip through the CT chamber and channels as shown in Figure 7. As the compressor back pressure is increased towards the design and stall point, the static pressure at the interface of CT duct and rotor casing is also increased and leads to almost zero mass flow rate going through the CT channels at the design point, Figure 8. When the micro-compressor is throttled beyond the design point, the flow goes from the rotor casing to the upstream inlet and returns with the main flow to the rotor blade as shown in Figure 9. When the compressor is throttled beyond point *C*, at which the compressor without CT is stalled, the flow in the compressor tip also goes upstream to the inlet, but is mixed with the large flow separation and does not return directly to the rotor inlet, as shown in Figure 10.

In order to understand the mechanism behind the extension of stall margin with CT, it is important to examine the effect of CT on the blockage area. At a high pressure ratio beyond the design point, with rise in the back pressure the flow through CT increases. When this recirculating flow mixes with the main flow in inlet duct near casing, angular momentum is exchanged due to the turbulence mixing. That causes flow to align more axially in the tip clearance region of the rotor leading edge and shrinkage of high negative axial velocity region near tip leading edge, Figure 11. Apart from the improvement near the leading edge of rotor in tip clearance region, overall field improves in the passage which is evident by delaying low axial velocity region on pressure side and similarly the shrinkage of low axial momentum region on both side of rotor blade with CT.

Low relative total pressure region on suction side of rotor blade can help to track the trajectory of the tip leakage flow. Figure 12 shows tip leakage trajectory with relative total pressure at five different sections in streamwise direction in rotor passage. From the Figure 12, it can be seen that at point *C* (as shown in Figure 12(a)) tip leakage vortex is still moving downstream in the main flow passage whereas near the stall point (Figure 12(b)) tip leakage vortex is creating blockage near the leading edge.

Radial Profiles

Circumferential mass averaged radial distributions of inlet meridional velocity, total pressure ratio and inlet flow angle for the rotor, diffuser and OGV are shown in Figures 13 to 15 for three different operating points. U_∞ in Figures 13(a), 14(a) and 15(a) refers to the velocity at inlet boundary condition. The inlet flow angle in Figures 13(c), 14(c) and 15(c) refers to the relative flow angle (β) for the rotor and the absolute flow angle (α) for the diffuser and OGV. At low pressure ratio, the inlet flow angle profiles (Figure 13(c)) for the rotor with/without CT show similar distribution but the inlet flow angle is slightly higher across the span with the casing treatment. Due to the less negative incidence angle for the compressor with CT, it ingests the mass flow rate lower than the compressor without CT, Figure 5. This can also be seen from the reduced meridional velocity across the span with the CT case. This change in incidence angle

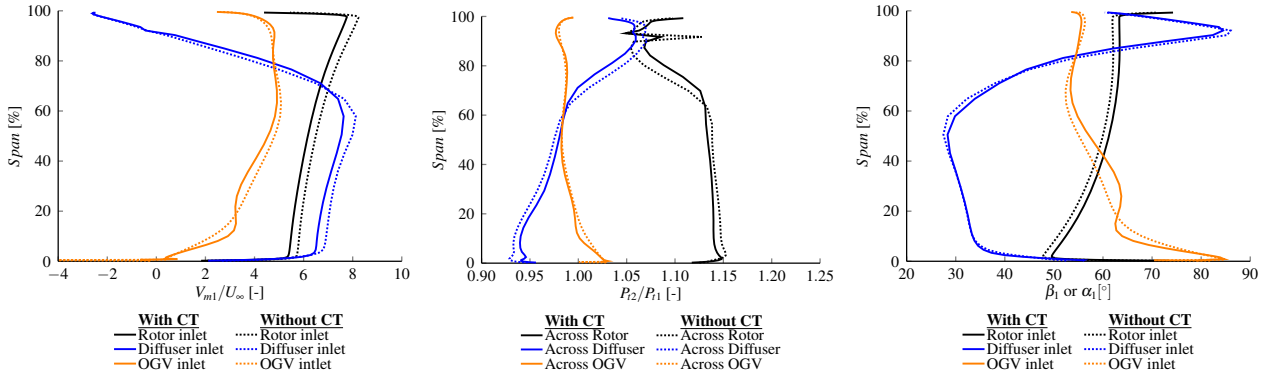

(a) Inlet meridional velocity (b) Total pressure ratio (c) Inlet flow angle

FIGURE 13: Radial Profiles at $Ps/Pt = 1.066$

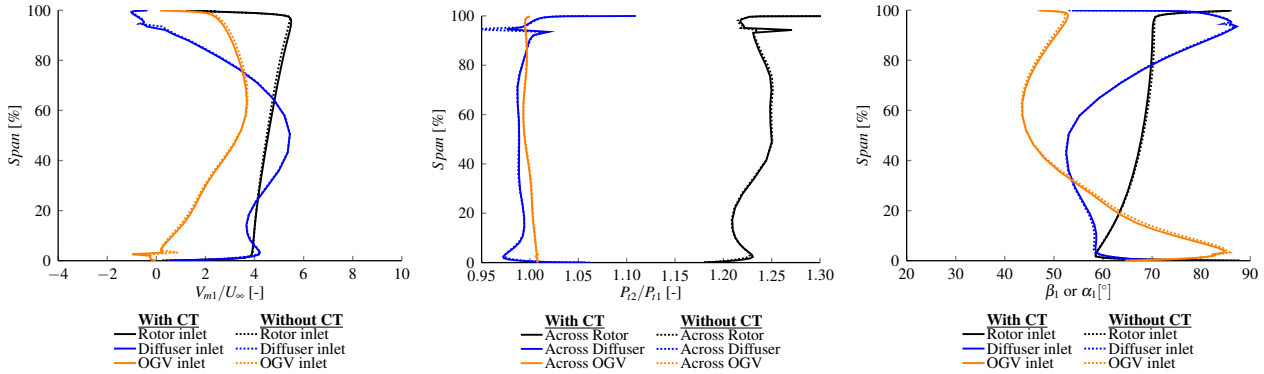

(a) Inlet meridional velocity (b) Total pressure ratio (c) Inlet flow angle

FIGURE 14: Radial Profiles at $Ps/Pt = 1.205$

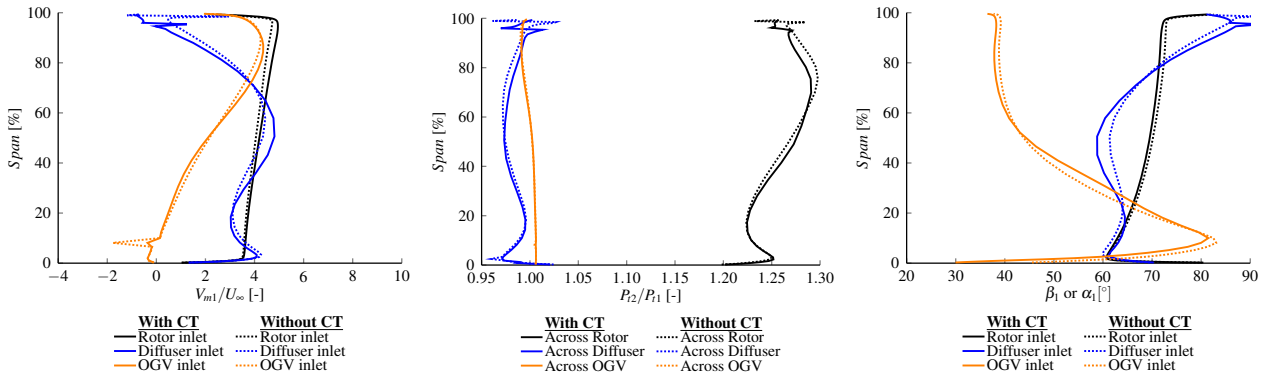

(a) Inlet meridional velocity (b) Total pressure ratio (c) Inlet flow angle

FIGURE 15: Radial Profiles at $Ps/Pt = 1.22$

is responsible for the lower mass flow rate with the CT case even though the throat area is the same for the compressor with and without CT. For the total pressure ratio profile, the case with CT has more work input to the flow in the tip region than the case with no CT. The total temperature ratio appears to be insensitive to the CT near the choke point.

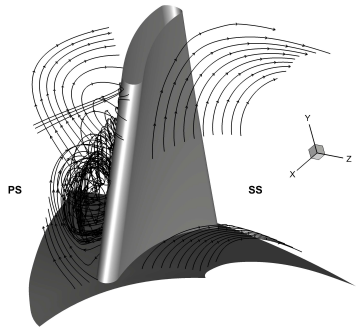

(a) $Ps/Pt = 1.066$

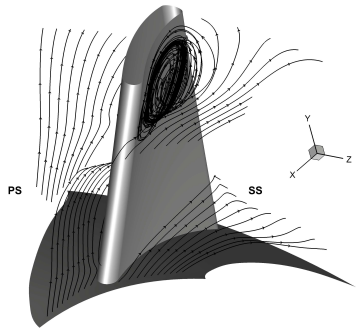

(b) $Ps/Pt = 1.22$

FIGURE 16: Flow separation in diffuser with CT

Near the design point, as recirculation mass flow through the CT channels is nearly zero, the CT has little effect and the radial distributions of the three flow quantities are about the same as shown in Figure 14.

As P_s/P_t is increased to 1.22, the increase in the meridional velocity and decrease in the inlet flow angle in the upper and mid span of the rotor inlet is observed. This is the indication that the CT is able to reduce the tip clearance flow blockage when the compressor is throttled to near stall. However, at the diffuser inlet, more mass flow is moved to near the mid span region due to the high momentum loss of the flow at casing for the high curvature turning. Reduction in rotor blade load can be observed above 65% span due to the blockage relief by the casing treatment that extends the compressor operating range. This effect of total pressure redistribution with CT case is also observed with the total temperature ratio profile.

Overall rise in stagnation quantities across the rotor can be seen for all the operating points due to the work done on fluid where as drop in total quantities is evident for the diffuser and OGV (Figures 13 to 15). Figure 16 shows the flow separation in diffuser passage at different pressure ratio. It can be seen that near the choke point (as shown in Figure 16(a)), pressure side of diffuser blade experiences large separation where as at $P_s/P_t = 1.22$ (as shown in Figure 16(b)) suction side experiences separation near the casing region.

Blade loading

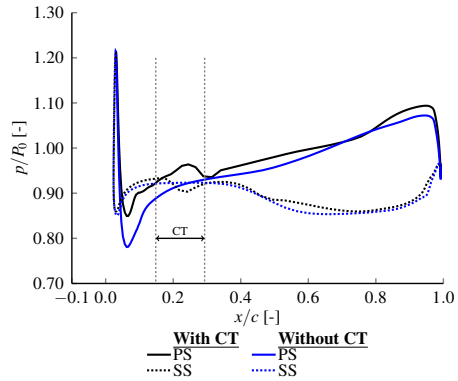

(a) At $Ps/Pt = 1.066$

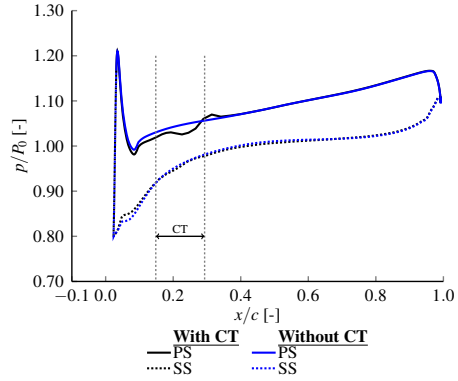

(b) At $Ps/Pt = 1.205$

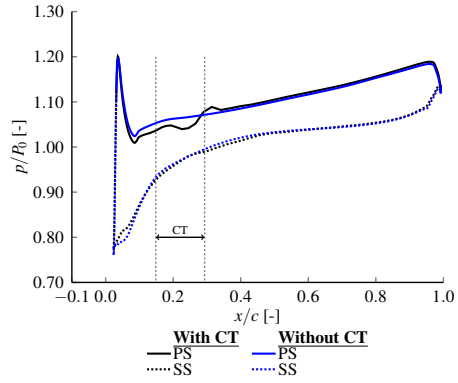

(c) At $Ps/Pt = 1.22$

FIGURE 17: 96.0% Span Blade loading

Figure 17 illustrates the blade tip loading at different operat-

ing points, where the blade static pressure is normalized with the total pressure at inlet. For the near choked point shown in Figure 17(a), a negative incidence angle caused by the CT flow entering the tip region produces negative work at the leading edge region.

With the increase in back pressure towards the design point from choke point, incidence angle changes from negative to positive. Figure 17(b) represents the blade static pressure distribution near the design point. Overall, the chordwise loading distribution between the with and without CT is very similar due to the near zero mass flow influence from the CT channels. A small effect of CT can be seen near the leading edge and in the CT area. The static pressure on the pressure surface for the CT case is reduced upto $0.28x/c$ and is followed by slight increase in very small region after CT.

With further increase in pressure ratio (Figure 17(c)), the incidence and the overall loading are further increased for both the case with and without CT. However, the one with CT has less incidence increase due to the CT relief of blockage, which results in a smaller loading and better flow condition.

CONCLUSION

The implementation of a FEM type interpolation for non-matching mesh interface is validated with the experimental results for the compressor with casing treatment. Extension in compressor operating range is investigated. The conclusions are drawn below:

1 The non-matching mesh interface does not achieve flux conservation. However mesh refinement helps to alleviate this discrepancy and the overall results are satisfactory.
2 At the near choked point, the self recirculating casing treatment has the flow entering the rotor tip from the upstream inlet due to the low back pressure. The effect of CT on mass flow rate, pressure ratio and efficiency near the design point is insignificant due to little flow going through the CT channels.
3 As the back pressure is increased to near stall condition, the CT channels relieve the tip region pressure by having the flow going upstream to the compressor inlet. This CT flow traveling upstream helps to reduce the flow blockage caused by tip vortex and thereby move its trajectory to more axial.
4 The CT flow traveling upstream reduces the incidence angle and improves flow condition by alleviating the blade tip loading.

ACKNOWLEDGMENT

All the computations were carried out using the computational resources of Center for Computational Science at University of Miami. We would also like to thank Mr. Chris Robinson of PCA Engineers and Mr. Christof Zwyssig of Celeroton AG for their fruitful discussion.

REFERENCES

[1] Zha, G., Paxton, C., Conley, C., Wells, A., and Carroll, B., 2006. "Effect of injection slot size on the performance of coflow jet airfoil". *AIAA Journal of Aircraft,* ***43***(4), July, pp. 987–995.
[2] Zha, G., Gao, W., and Paxton, C., 2007. "Jet effects on coflow jet airfoil performance". *AIAA Journal,* ***45***(6), June, pp. 1222–1231.
[3] Zha, G., Carroll, B., Paxton, C., Conley, C., and Wells, A., 2007. "High-performance airfoil using coflow jet flow control". *AIAA journal,* ***45***(8), Aug., pp. 2087–2090.
[4] Lefebvre, A., Dano, B., Bartow, W., Fronzo, M., and Zha, G., 2016. "Performance and energy expenditure of coflow jet airfoil with variation of mach number". *Journal of Aircraft,* ***53***(6), June, pp. 1757–1767.
[5] Gan, J., Im, H., and Zha, G., 2016. "Delayed detached eddy simulation of rotating stall for a full annulus transonic axial compressor stage". ASME No. GT2016-57985.
[6] Hathaway, M., 2002. "Self-recirculating casing treatment concept for enhanced compressor performance". ASME No. GT2002-30368.
[7] Chen, H., and Lei, V., 2012. "Casing treatment and inlet swirl of centrifugal compressors". *Journal of Turbomachinery,* ***135***(4), Sept. Paper No: TURBO-12-1109.
[8] Shabbir, A., and Adamczyk, J., 2004. "Flow mechanism for stall margin improvement due to circumferential casing grooves on axial compressors". ASME No. GT2004-53903.
[9] Hembera, M., Kau, H., and Johann, E., 2008. "Simulation of casing treatments of a transonic compressor stage". *International Journal of Rotating Machinery,* ***2008***, Oct. Article ID 657202.
[10] Khalid, S., 1997. "A practical compressor casing treatment". ASME No. 97-GT-375.
[11] Yang, M., Martinez-Botas, R., Zhang, Y., and Zheng, X., 2016. "Effect of self-recirculation-casing treatment on high pressure ratio centrifugal compressor". *Journal of Propulsion and Power,* ***32***(3), Jan., pp. 602–610.
[12] Yang, C., Zhao, S., Lu, X., Han, G., and Zhu, J., 2014. "Investigation on multiple cylindrical holes casing treatment for transonic axial compressor stability enhancement". *Journal of Thermal Science,* ***23***(4), Aug., pp. 346–353.
[13] Zha, G., Yang, Y., Ren, Y., and McBreen, B., 2018. "Superlift and thrusting airfoil of coflow jet actuated by micro-compressors". In 2018 Flow Control Conference, American Institute of Aeronautics and Astronautics.

[14] Benek, J., Steger, J., Dougherty, F., and Buning, P., 1986. Chimera: A grid-embedding technique, Apr.

[15] Kao, K., and Liou, M., 1995. "Advance in overset grid schemes: From chimera to dragon grids". *AIAA Journal,* ***33***(10), Oct.

[16] Fenwick, C. L., and Allen, C. B., 2006. "Development and validation of sliding and non-matching grid technology for control surface representation". *Proceedings of the Institution of Mechanical Engineers, Part G: Journal of Aerospace Engineering,* ***220***(4), pp. 299–315.

[17] https://turbmodels.larc.nasa.gov/spalart.html.

[18] Allmaras, S., Johnson, F., and Spalart, P., 2012. "Modifications and clarifications for the implementation of the spalart-allmaras turbulence model". No. ICCFD7-1902, Seventh International Conference on Computational Fluid Dynamics (ICCFD7).

[19] Wang, B., 2009. "Detached-eddy simulation of flow nonlinearity of fluid-structural interactions using high order schemes and parallel computation". phdthesis, University of Miami, Coral Gables, May.

[20] Hutton, D., 2004. *Fundamentals of Finite Element Analysis*, 1 ed. McGraw Hill.

[21] Im, H., Chen, X., and Zha, G., 2012. "Detached-eddy simulation of rotating stall inception for a full-annulus transonic rotor". *Journal of Propulsion and Power,* ***28***(4), July.

[22] Zha, G., 1999. "Comparative study of upwind scheme performance for entropy condition and discontinuities". 14th Computational Fluid Dynamics Conference. American Institute of Aeronautics and Astronautics, July.

[23] Wang, B., and Zha, G., 2008. "Comparison of a low diffusion e-cusp and the roe scheme for rans calculation". 46th AIAA Aerospace Sciences Meeting and Exhibit. American Institute of Aeronautics and Astronautics, Jan.

[24] van Leer, B., 1979. "Towards the ultimate conservative difference scheme. v. a second-order sequel to godunov's method". *Journal of Computational Physics,* ***32***(1), pp. 101 – 136.

[25] Wang, B., Hu, Z., and Zha, G., 2008. "A general subdomain boundary mapping procedure for structured grid cfd parallel computation". *AIAA Journal of Aerospace Computing, Information, and Communication,* ***5***, pp. 425–447.

[26] Robinson, C., 2017. Design of a mixed flow fan. PCA engineers Limited, Internal Report to University of Miami, PCA-211-3-rep1-1, Feb.

[27] Zwyssig, C., 2017. Design of a mixed flow fan prototype. Final Contract Report to University of Miami, PR-4241-001, Oct.